Angewandte Chemie International Edition

Angewandte International Edition Chemie

How to cite: *Angew. Chem. Int. Ed.* **2026**, e9945587
doi.org/10.1002/anie.9945587

RESEARCH ARTICLE OPEN ACCESS

Spiro-Linked Double Tetraphenylethenes: Solid-State Emission and Circularly Polarized Luminescence Imaging

José L. Páez[1] | Riccardo Rubino[2] | Giulia Micolonghi[3] | Marco Reale[2] | Alice Sciortino[2] | Victor Blanco[1] | Angel Orte[3] | Carlos M. Cruz[1]

[1]Department of Organic Chemistry, Unidad De Excelencia de Química (UEQ), Faculty of Sciences, University of Granada, Granada, Spain | [2]Department of Physics and Chemistry (DiFC) "E. Segrè", University of Palermo, Palermo, Italy | [3]Nanoscopy-UGR Laboratory. Department of Physical Chemistry, Unidad De Excelencia de Química (UEQ), Faculty of Pharmacy, University of Granada, Granada, Spain

Correspondence: Angel Orte (angelort@ugr.es) | Carlos M. Cruz (cmorenoc@ugr.es)

Received: 31 January 2026 | **Revised:** 17 April 2026 | **Accepted:** 21 April 2026

Keywords: circularly polarized luminescence | fluorescence spectroscopy | polycycles | spiro compounds | time-resolved spectroscopy

ABSTRACT

Herein, we report the synthesis and structural characterization of two spiro-linked tetraphenylethenes and investigate their optical properties in solution, as aggregates, and in the solid state. This family comprises two double spirobisanthracene-tetraphenylethene hybrid systems. Approaching the synthesis and understanding the structure of these unexplored spiro-systems opens the door to studying their properties both in solution and in the solid state. Besides the structural novelty of the prepared compounds, their solid-state optical properties are remarkable. White and blue emissions are observed in the double spirobisanthracene-tetraphenylethene hybrid derivatives. In addition, one of the synthesized compounds is chiral, and separation of its enantiomers enable the study of their chiroptical properties, revealing circularly polarized luminescence in films, aggregates and dispersions. Crystals were analyzed via circularly polarized luminescence microscopy, allowing the identification of racemic and enantiopure crystals via single-particle analysis. This work paves the way for a further extension of the spirobisanthracene capabilities toward their implementation in emissive devices.

1 | Introduction

Spirocompounds are a family of organic molecules composed of two cycles that share a common central tetrahedral atom. Spiro-linkage is useful to connect two different π-conjugated structures through a non-conjugated central atom [1]. In this sense, spiroconjugation may arise, influencing the electronic distribution of the linked π-systems, and providing a tool to modulate their optoelectronic properties [2–7]. Carbon-based spirocompounds are of special interest due to the structural versatility of carbon compared to other elements. Spirobifluorene (SBF) has been deeply studied [8] and is currently part of commercially available and widely used hole transport material in solar cells [9–11], among other applications [12]. Currently, pure hydrocarbon SBF derivatives are under study, with a current focus on extending the conjugated structure [13–19], or the preparation of SBF monomers, dimers and trimers as hosts matrices for emissive devices [20–22]. In this sense, the insertion of two double benzylic carbons into SBF can generate a dihydro spirobisanthracene (SBA, Figure 1) scaffold. The extra benzylic positions in SBA can be used to extend the conjugated structure and, thus, connect different types of π-systems through a spirocenter. Surprisingly, SBA-related systems are still underexplored, with only a few examples reported in the literature. SBA-diones have shown potential as stabilized triplet excited states [23], while polyspirocenters based on SBA have only recently been prepared [24]. With this background, we explored the possibility of linking two functional π-systems through an SBA scaffold. As proof

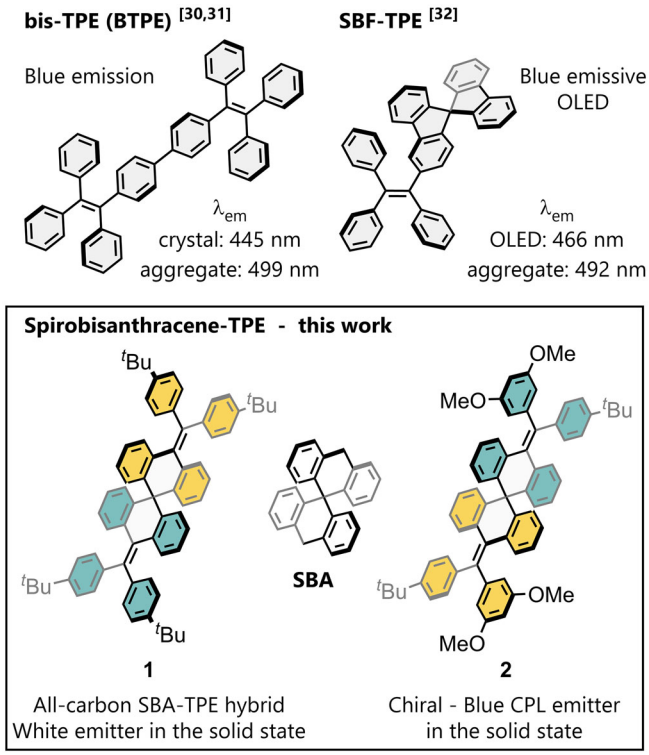

FIGURE 1 | Top: Structures of BTPE, as an all-carbon double TPE molecule, and SBF-TPE as an example of spiro-TPE hybrid molecule reported in the literature. Bottom: structure of SBA and structures of the prepared spirobisanthracene-TPE hybrid molecules reported herein and their main features.

of concept, we selected tetraphenylethene (TPE) [25]. TPE is a well-known π-system exhibiting aggregation induced emission (AIE) [26, 27], which has enabled a plethora of applications [28]. The TPE moiety has been used as a building block of many different architectures, such as macrocycles and cages with different number of TPE units [29]. TPE dimers, such as 4,4'-bis(1,2,2-triphenylvinyl)biphenyl (BTPE, Figure 1), have also shown interesting properties, including outstanding fluorescence quantum yield (Φ_F) and deep blue AIE [30, 31]. However, carbon-based spiro-TPE hybrids are underexplored, and only a single reported example based on a SBF-TPE hybrid can be found in literature (SBF-TPE, Figure 1) [32], whereas spiro-TPE hybrids bearing heteroatoms are more common [33]. Therefore, we envisage SBA as the central scaffold to explore new all-carbon spiro-TPE hybrid systems. The SBA π-systems can be regarded as two half TPE moieties, which, by exploiting the benzylic positions, can be completed to form full TPE units. With this idea in mind, we proposed the synthesis of compounds **1** and **2** (Figure 1) and the study of their structural and optical properties in solution and the solid state. Compounds **1** and **2** are designed as SBA-TPE analogues bearing two TPE units. Additionally, we took advantage of the SBA unit to introduce chirality in analogue **2** (Figure 1) and enable the study of its chiroptical properties. In particular, circularly polarized luminescence (CPL) response was evaluated for compound **2** in aggregates, films, dispersions, and crystals. The latter was examined through CPL imaging [34, 35] as one of the few examples of organic molecules detected using this technique [36].

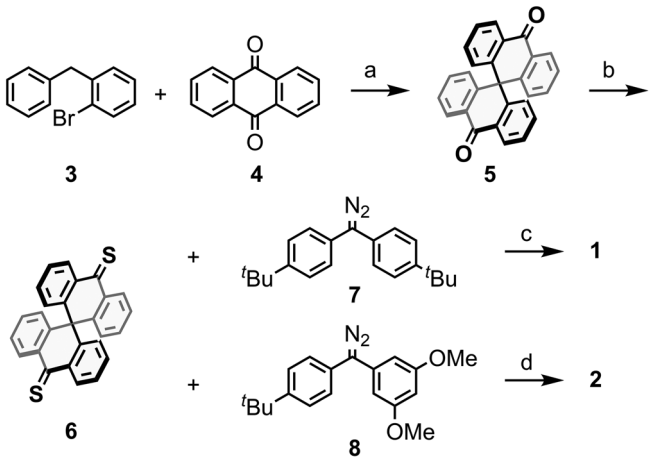

SCHEME 1 | Synthesis of compounds **1** and **2**. Reagents and conditions:(a) (i) *n*BuLi, THF, −78°C to RT, 16 h, (ii) $MeSO_3H$, CH_2Cl_2, RT, 16 h, (iii) $KMnO_4$, MeCN, 60°C, 16 h; (b) Lawesson's reagent, toluene, 110°C, 16 h; (c) PPh_3, *m*-xylene, 140°C, 1 h; (d) PPh_3, *m*-xylene, 140°C, 2 h.

2 | Results and Discussion

2.1 | Synthesis and Structural Characterization

Compounds **1** and **2** were synthesized according to Scheme 1. Starting from 2-bromodiphenylmethane **3**, and anthraquinone **4**, spirobisanthracene dione **5** was prepared, using a modified reported strategy (Scheme 1) [23]. Compound **5** was transformed into its corresponding dithione **6** using Lawesson's reagent. Subsequent Barton–Kellogg reaction with diazo derivative **7** yielded compound **1**. Using an analogous strategy, the chiral derivative **2** was prepared using diazo derivative **8** during the Barton–Kellogg reaction (Scheme 1).

Compounds **1** and **2** were isolated as white powders. Their structures were confirmed by nuclear magnetic resonance spectroscopy (NMR), high-resolution mass spectrometry (HRMS), and by single crystal x-ray diffraction (SCXRD) (Supporting Information). According to SCXRD, the SBA moiety of **1** and **2** shows a boat-like conformation in the two anthracene moieties (Figure 2) with a bent angle (θ) of 62° and 56° for **1** and **2**, respectively. This is in accordance with the DFT optimized geometries, θ = 56° and 58°, respectively (B3LYP/6-31G(d,p)). The two possible boat-like conformations can be interconverted by reverse folding with a calculated energy barrier of 6.4 kcal mol^{-1} for **1** (B3LYP/6-31G(d,p), Figure S54), suggesting that the process takes place at room temperature. This calculated energy barrier is lower than the one observed in 10,10-dimethyl-9,10-dihydroanthracenes [37], suggesting that the presence of the second anthracene moiety and the *p-tert*-butylphenyl substituents contribute to a higher energy ground state. Two energy barriers of 6.9 and 6.5 kcal mol^{-1} were calculated for **2** (Figure S58), which interconvert their three identified conformers (Figure S55–S57). Aromaticity indexes were analyzed through the harmonic oscillator model of aromaticity (HOMA) and the nucleus independent chemical shift (NICS). The HOMA and $NICS(0)_{iso}$ show expected values for the Clar sextets of **1** and **2**, while the central rings of the SBA moiety show a marked non-aromatic character (Supporting Information,

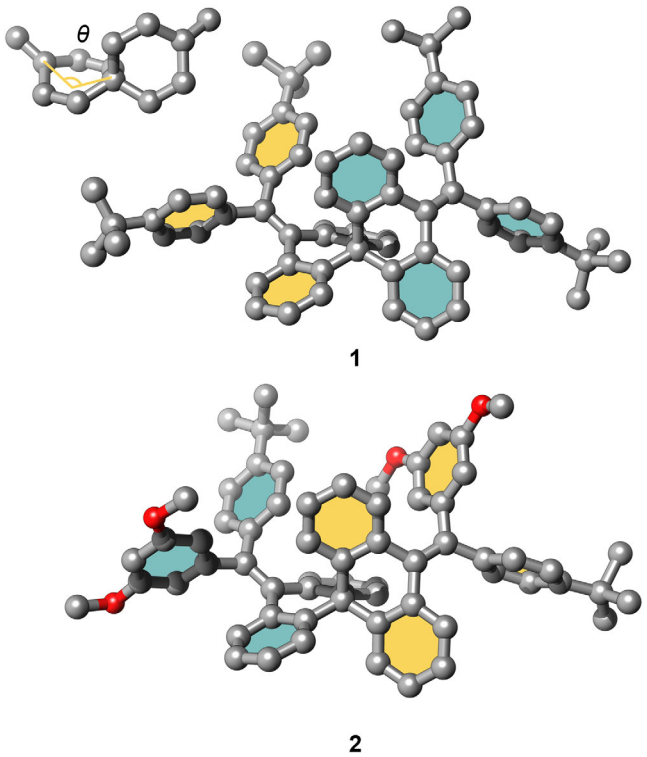

FIGURE 2 | Single crystal x-ray diffraction structures of compounds **1–2**. Top left: schematic representation of the measured angle θ. Color code: C, gray; O, red. Hydrogen atoms and disorder of some ^{t}Bu groups are omitted for clarity [38].

Figure S68). Frontier molecular orbitals (FMOs) of **1** are extended over the entire molecule, while they are mostly located at the 3,5-dimethoxyphenyl (HOMO) and the SBA (LUMO) moieties in compound **2** (Figures S59–S61).

2.2 | Solid-State Emission

Solutions of **1** and **2** in THF exhibited absorption in the UV region (270–390 nm), with maxima at 303 and 289 nm, respectively. The molar absorption coefficient (ε) was evaluated as 2.50×10^4 and 2.48×10^4 L mol^{-1} cm^{-1} at the maxima, respectively (Figures S31–S33). Remarkably, compound **2** shows a hypsochromic shift compared to **1**.

TPE-related compounds are well-known for their AIE properties. Hence, we probed the emission properties of **1** and **2** upon increasing the volume fraction of water (f_w) in THF solutions. Aggregation caused notable spectral changes in **1** from $f_w = 70\%$, ranging from the appearance of a red band at 625 nm to, eventually, the arising of broad white emission in a dispersion of $f_w = 99\%$ (Supporting Information, Figure S35). The resulting CIE1931 coordinates (x,y) of this emission profile are (0.306, 0.321), which match those of the daylight illuminant standard D65 (0.313, 0.329) (Figure S48). We analyzed the 99:1 (v/v H_2O/THF) dispersion of **1** by TEM imaging, finding amorphous aggregates (Figure S49). Similar behavior was found for **2**, where the emission in a 99:1 (v/v H_2O/THF) dispersion was slightly blueshifted (Figure S36). The CIE1931 coordinates of this emission profile are (0.250, 0.225) (Figure S48). We measured the fluorescence emission decay traces of those aggregates in a 99:1 (v/v H_2O/THF) mixture, using time-resolved fluorimetry, and obtained multiexponential behavior varying along the emission band. The average lifetime values of **1** varied from 1.3 ± 0.1 ns at 450 nm to 3.7 ± 0.2 ns at 550 nm whereas for compound **2** the lifetimes were 5.0 ± 0.1 ns at 450 nm and 6.0 ± 0.1 ns at 550 nm (Figures S37 and S38; Table S2). Interestingly, compound **2** exhibited complex excited-state dynamics, evidencing the formation of red emissive excimers, with long lifetime values. The broad-band emission of aggregates from **1** and **2** was measured by multichannel confocal fluorescence lifetime imaging (FLIM). We probed the emission of aggregates deposited on glass slides over three detection channels for blue (450 nm), yellow (550 nm), and red (630 nm) emission upon excitation at 375 nm (Figure S42), and built the ratiometric images, I_{450}/I_{550}, I_{630}/I_{550} and I_{630}/I_{450}, the later representing the excess of red emission. Figure S31B,C show images of dispersed aggregates of **1** and **2** in a 99:1 (v/v H_2O/THF) mixture. A particle-wise quantification of the images demonstrated that aggregates of **1** have higher I_{630}/I_{450} ratio values than **2**, indicating that **1** exhibits a broader emission band in the aggregate state. Moreover, the aggregates of **1** exhibited a size-dependent I_{630}/I_{450} ratio, with larger values for larger and brighter aggregates (Figure S42D), indicating that the red emission is favored upon aggregation.

We then analyzed the solid-state emission of crystals of **1** and **2**. FLIM imaging of crystals of **1** and **2** showed striking differences. On the one hand, **1** crystalized in the form of large flake-like crystals, but small fragments were also detected (Figure 3A). These crystals exhibited low lifetime values, indicating that packing fostered emission quenching. In contrast, compound **2** exhibited two morphologically different types of crystals: small flake-like and needle-shaped ones (Figure 3A). Importantly, these two different types of crystals exhibited different lifetime values, whereas flakes showed low lifetime values, similar to compound **1**, the needle-shaped crystals had much larger lifetime values, indicating a structurally different packing that fostered emission. We performed a particle-wise analysis of the FLIM images in three detection channels (450/40, 465/35, and 630/60 nm; where xxx/yy refers to: xxx = center of the band, yyy = width of the band) to extract lifetime values from different crystal fragments and reconstruct lifetime distributions (Figure 3B). Whereas flake-shaped crystals of **1** showed consistent lifetime values of 1.1 ± 0.2 ns, with slightly larger values in the red-emission region, lifetime distributions of compound **2** fragments clearly exhibited three distinct lifetime populations that correlate with the different shapes and thus packing structures. Flake-like crystals showed lifetime values of 2.1 ± 0.3 ns, whereas needle-shaped crystals exhibited two populations with lifetimes of 4.1 ± 0.1 and 6.6 ± 0.1 ns. Interestingly, needle-crystals emitted with the shortest lifetime at the short wavelengths, whereas they preferentially emitted with the long lifetime at 630 nm. Moreover, the different crystals showed differences in the spectral distribution and thus on intensity ratio images (Figure 3C,D). Figure 3C shows I_{630}/I_{450} ratio images of crystals of **1** and **2**. Flake-like crystals of compound **1** exhibited I_{630}/I_{450} intensity ratio values of 2.6 ± 0.3, and 3.1 ± 0.7 for flakes of compound **2**. In contrast, needle-like crystals of **2** showed an I_{630}/I_{450} ratio of 5.1 ± 0.7 (Figure 3D).

All these features indicated that needle-shaped crystals of **2** contain two different emissive states in the broad-band emission.

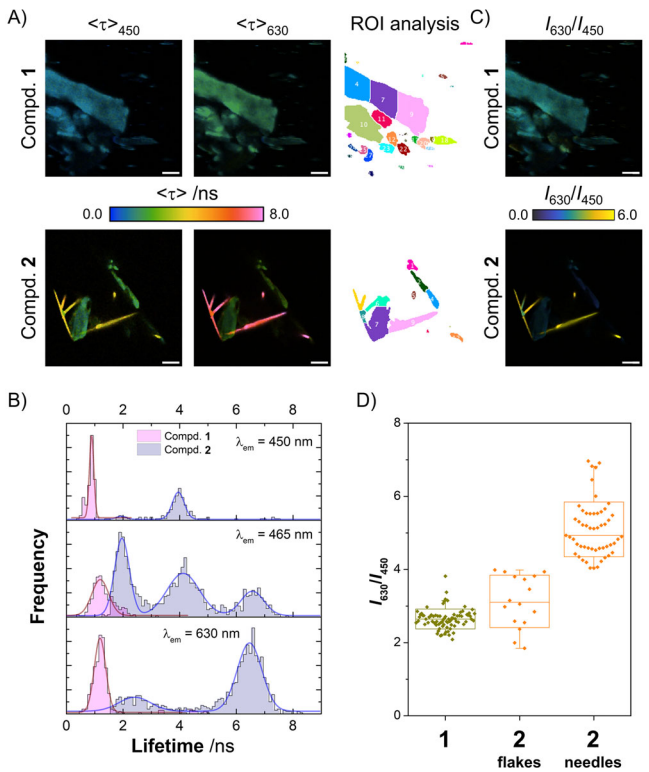

FIGURE 3 | (A) Representative FLIM images in the 450 nm and the 630 nm channels of crystals of compounds **1** and **2** suspended in DMF:MeOH. Scale bars represent 10 μm; (B) Automatic particle-wise analysis is performed to select different ROIs for extracting lifetime distributions. The lifetime histograms reconstructed from all images of compound **1** (pink histograms) and **2** (blue histograms) in the 450, 465, and 630 nm channels were fitted to 1, 2, or 3 gaussian functions. Box plots show the distribution of lifetimes in the different ROIs from all images collected in the three channels. Boxes represent std dev, whereas whiskers represent 95% of events. (C) I_{630}/I_{450} ratio imaging, on a pseudocolor scale, of the images in (A); (D) Box plot of average I_{630}/I_{450} ratio values from different images of crystals of compounds **1** and **2**. Boxes represent std dev, whereas whiskers represent 95% of events.

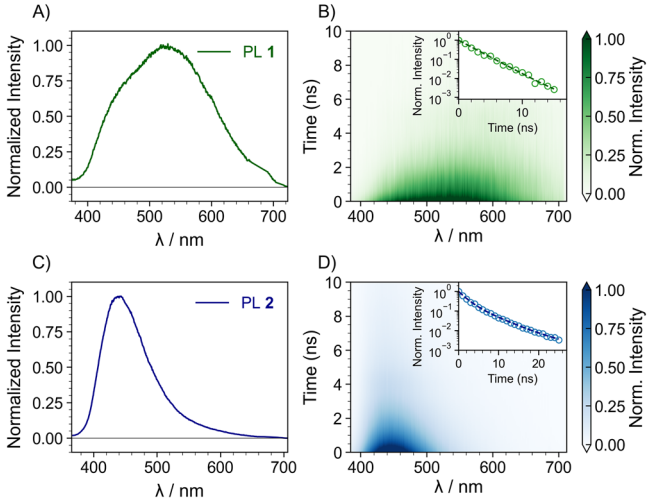

FIGURE 4 | Steady-state and time-resolved photophysical characterization of **1** (panels A and B) and **2** (C and D) in the solid state (thin films).(A and C) Steady-state photoluminescence of compounds **1** and **2** collected with λ_{exc} = 340 nm. A linear interpolation was applied in the region around 680 nm to eliminate artifacts due to scattered laser light. (B) and (D) False-color intensity maps of time-resolved emission as a function of wavelength and delay after excitation; insets show decay traces obtained by integrating the emission over the entire spectral band with corresponding fits.

Red-shifted, long-lived emission was likely caused by excimer-like interactions, whereas the monomeric state preferentially emitted in the blue region of the spectrum. However, these are striking differences with respect to the emissive features of the aggregates formed in H_2O/THF (99:1 v/v) mixtures. Flake-like crystals of **1** result in self-quenched, blueshifted emission, indicating a different packing motif than that of the aggregates. These observations were supported by spectral measurements combined with the confocal, obtaining spectra from the different crystals of **1** and **2** (Figure S41).

This observation led us to analyze the solid-state emission of compounds **1** and **2** in the form of powder pellets. Figure 4A shows the steady-state photoluminescence of **1** in the solid state under near-UV excitation at 340 nm. As can be seen, compound **1** displays a broad emission spanning an extremely wide spectral range (400–700 nm) yielding a white-light appearance. This intense solid-state luminescence is consistent with the well-established restriction of intramolecular motion mechanism characteristic of TPE-based emitters. Upon aggregation and crystallization, restricted molecular mobility suppresses non-radiative relaxation pathways associated with intramolecular rotations of the peripheral phenyl rings and other torsional motions, including twisting of the central C=C bond [39]. Time-resolved photoluminescence measurements (Figure 4B) demonstrate substantial temporal evolution during the decay, with pronounced progressive changes in spectral shape (Figure S39A,B) and wavelength-dependent decay kinetics (Figure S40A). These features, in agreement with the results from aggregates in 99:1 (v/v H_2O/THF), are a sign that the white-light photoluminescence arises from the superposition of multiple emissive components with distinct decay dynamics. This behavior is consistent with a heterogeneous system in which multiple chromophoric species contribute to the overall emission, likely associated with different molecular aggregates, packing motifs, or conformational states of compound **1** in the solid state. A similar coexistence of multiple emissive states has been reported in other AIE-active systems with sterically demanding scaffolds, where high-energy locally excited states and lower-energy excimer or aggregate states contribute simultaneously to a broad, white-light emission [40, 41]. In our case, the SBA scaffold is expected to prevent uniform close packing, favoring a distribution of heterogeneous environments that give rise to multiple emissive species. Despite this complexity, the decay kinetics of **1** (Figure 4B, inset) obtained by integrating the emission over the entire spectral band, can still be satisfactorily described by a single-exponential function with a lifetime in the nanosecond range (~2.5 ns, Table S3), characteristic of highly dipole-allowed optical transitions. This apparent mono-exponential behavior reflects the dominance of long-wavelength emission components, which persist significantly longer than the shorter-wavelength contributions, as can be seen from the detailed wavelength-resolved analysis in Figure S40A, with the results shown in Table S3. Interestingly, the different nature of the

FMOs of compounds **1** and **2** leads to significant changes in their solid-state optical response, despite the structural differences between the two being subtle. Indeed, Figure 4C shows that compound **2**, although still exhibiting a broad emission, displays a somewhat narrower spectral profile characterized by a more pronounced peak in the blue region (around 440 nm). Besides, the decay dynamics of this solid-state emission (Figures 4D and S39C,D) still display spectral evolution during decay, confirming contributions from different emitters, but this effect is much less pronounced compared to compound **1**. The decay kinetics of **2** require a bi-exponential fitting function to adequately describe the temporal evolution (Figure 4D, inset), revealing the presence of at least two well-defined relaxation channels with lifetimes of 1.8 ± 0.3 and 5.2 ± 0.6 ns (Table S4), in excellent agreement with the values obtained from aggregates (Table S2). This multiexponential behavior and the distinct solid-state optical response between the two derivatives underscore the active photophysical role of the spiro-linkage. As established for related spiro-conjugated systems, the rigid 3D spiro core not only limits detrimental π–π stacking [33] but also participates in excited-state conformational relaxation [42]. Together, these effects strongly influence the energy landscape in the solid state, thereby modulating the relative contributions of monomeric and aggregate-derived emissive pathways.

2.3 | Chiroptical Properties and CPL Imaging

Compound **2** exhibits axial chirality. Therefore, its enantiomers were separated using chiral stationary phase high performance liquid chromatography (Figure S50). The electronic CD spectra of (*P*)- and (*M*)-**2** were measured in THF and shows a $|\Delta\varepsilon|$ of 10 L mol^{-1} cm^{-1} at 310 nm ($|g_{abs}| = 6.0 \times 10^{-4}$) (Figure 5A). The configuration was assigned with the help of TD-DFT calculations (B3LYP/6-31G(d,p)) according to the Boltzmann distribution of the three conformers (Figures S55–S57). The circularly polarized luminescence of (*P*)- and (*M*)-**2** was measured in aggregates from a 99:1 (v/v H_2O/THF) dispersion (Figure 5B), and in the solid state, both as a dispersion in KBr (Figure 5C) and in thin films (Figure 5D). The aggregates show a $|g_{lum}|$ of 2.5×10^{-3}. The dispersion in KBr exhibits a $|g_{lum}|$ of 2.5×10^{-4} at the emission maximum. Films of (*P*)- and (*M*)-**2** were prepared via drop casting, and their CPL was recorded in the 400–500 nm range, exhibiting a g_{lum} value in the range of 10^{-3}. Remarkably, the CPL sign of the enantiomers is inverted with respect to the lowest energy band of the CD spectra.

Given the detection of CPL emission of compound **2**, we also performed confocal imaging of circularly polarized dissymmetry by modifying the instrumentation (Supporting Information). In this mode, we used a $\lambda/4$ plate, with the fast axis set at +45°, set in the detection optical pathway and the emission was split by a polarizing cube in the horizontal (P) and vertical (S) components, collecting two images with the intensities in each channel (I_P and I_S, respectively) (Figure 6). Using this configuration, an excess of RCP emission resulted in an excess in the P component, whereas an excess of LCP emission yielded larger intensities in the S channel. Hence, by inspecting I_P/I_S ratio images, CPL dissymmetry can be detected. We applied this configuration using two different chromatic detection bands, at 465/30 nm for blue emission, and 630/60 nm for red emission (Figure 6A).

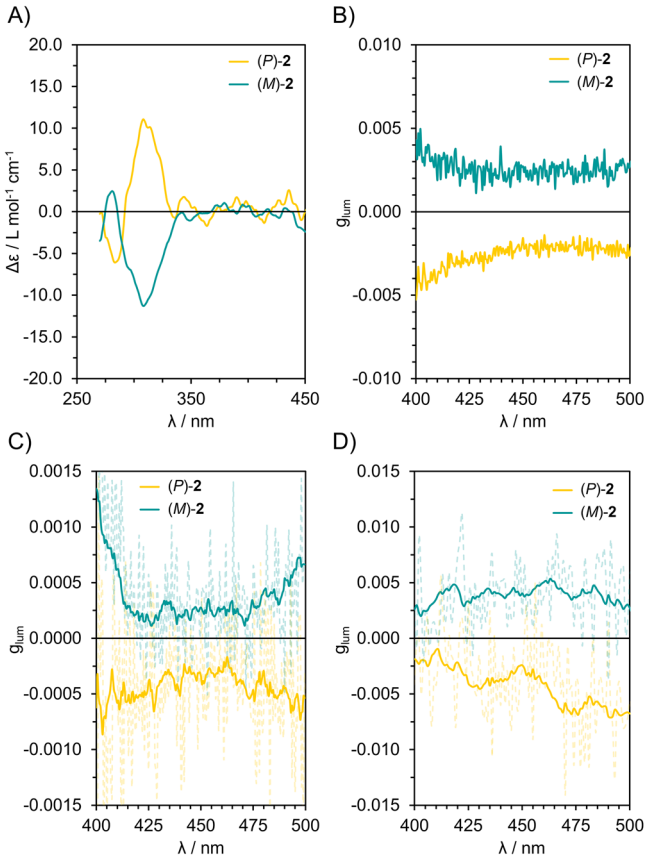

FIGURE 5 | (A) Electronic circular dichroism spectra of compounds (*P*)- (viridian) and (*M*)-**2** (yellow). (B) Dissymmetry factor of luminescence for (*P*)- (viridian) and (*M*)-**2** (yellow) measured in a 99:1 (v/v H_2O/THF) mixture. (C) Dissymmetry factor of luminescence for (*P*)- (viridian) and (*M*)-**2** (yellow) measured in KBr pellets, raw data is shown in dashed lines and smoothed data in solid lines. D) Dissymmetry factor of luminescence for (*P*)- (viridian) and (*M*)-**2** (yellow) measured in drop-casted thin films, raw data is shown in dashed lines and smoothed data in solid lines.

Flake crystals of compound **1** exhibited negligible dissymmetry, with I_P/I_S ratio values close to 1 (Figure 6B). However, crystals of **2** exhibited three distinct populations. While flake crystals were characterized by low dissymmetry values, needles exhibited either high I_P/I_S ratio values (corresponding to excess of RCP) or low I_P/I_S ratios (indicating excess of LCP emission). We employed the same automatic algorithm, as described in the FLIM section, for identification of regions of interest (ROIs) and obtaining the particle-wise I_P/I_S ratio distributions across all the images (Figure 6C). These distributions clearly illustrate that compound **1** only showed negligible dissymmetry, whereas compound **2** presented crystal fragments with LCP, RCP, and no CPL emission.

To ensure that these differences in emission polarization do not arise from artifacts, we collected the same FoVs but by rotating the fast axis of the $\lambda/4$ plate to −45°. Under this configuration, RCP light yields excess in the S component after the polarizing beam splitter, whereas LCP light results in an excess of the P component. Hence, $I_P/I_S < 1$ indicates RCP, whereas $I_P/I_S > 1$ arises from LCP (Figure 6A). Figure 6D illustrates that crystals of **1** did not notably undergo changes in the I_P/I_S ratio upon

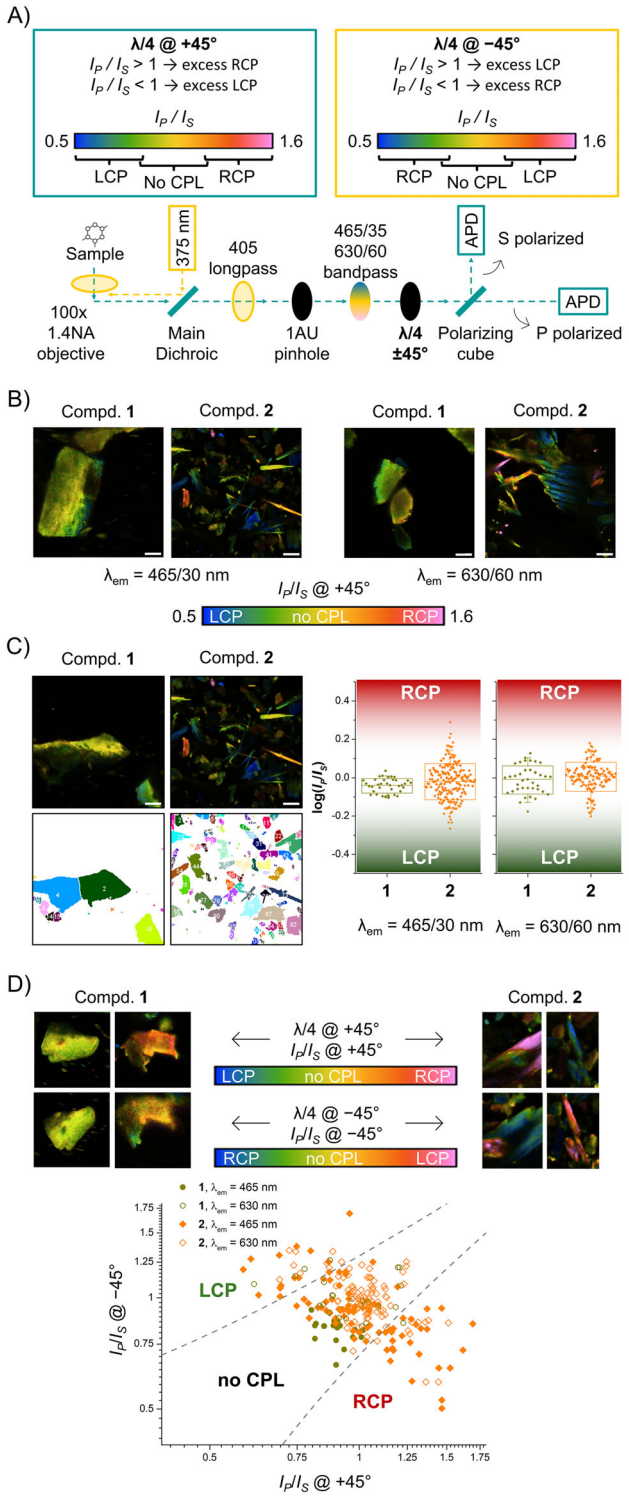

FIGURE 6 | (A) Scheme of the confocal microscopy instrumentation to measure emission CPL dissymmetry. The collected emission passes through a $\lambda/4$ plate, with the fast axis set at +45° or −45° and is split into the vertical (S) and horizontal (P) components. Ratiometric imaging reconstruction of the I_P/I_S ratio indicates excess of RCP or LCP, with high or low values correlated with the different chirality, depending on the orientation of the $\lambda/4$ plate. (B) Representative I_P/I_S ratio images of crystals of compounds **1** and **2** suspended in DMF:MeOH, in the 465/30 nm and the 630/60 nm bands, with the $\lambda/4$ plate set at +45°. Scale bars represent 10 μm. (C) Automatic particle-wise analysis was performed to select different ROIs for extracting I_P/I_S ratio distributions. Box plots show distribution of I_P/I_S ratio from crystal fragments of **1** (dark yellow) and **2** (orange) in the 465/30 nm (left) and the 630/60 nm (right) bands. Boxes represent std dev, whereas whiskers represent 95% of events. Note that a log scale is used because an intensity ratio is not a normal-distributed function. In contrast, the log of the ratio follows indeed a normal distribution. (D) Exemplary comparisons of I_P/I_S ratio images of crystal fragments of **1** and **2**, when the axis of the $\lambda/4$ plate is rotated from +45° to −45°. The plot correlates the I_P/I_S ratio values of crystal fragments of **1** (dark yellow symbols) and **2** (orange symbols) with the $\lambda/4$ plate set at +45° (x-axis) or −45° (y-axis). Closed symbols represent results from the 465/30 nm emission band, while open symbols are from results in the 630/60 nm band. APD: avalanche photodiode.

rotating the $\lambda/4$ plate, whereas crystals of **2** that exhibited high I_P/I_S ratio values correlated with low I_P/I_S ratios with the change in the direction of the $\lambda/4$ plate. Then, we correlated the I_P/I_S ratio values with $\lambda/4$ at +45° with the corresponding values when the $\lambda/4$ plate was set at −45°, for all the different particles in the images collected for compounds **1** and **2** (Figure 6D). This plot corroborates that compound **2** presented crystal fragments unequivocally emitting excess of RCP and other fragments emitting excess of LCP. Importantly, these features indicate a complex crystallization behavior of **2**, including crystallization-driven enantiomeric selection. The clearly different packing of needle-like crystals with respect to flake crystals appears to correlate with emission of CPL emission. Interaction and crystallization of different enantiomers should not emit CPL, thus flake crystals of **2** likely contain both (*M*)- and (*P*)-**2** enantiomers. However, emission of CPL should arise from chirality in the crystals, driven by enantiomeric selection during nucleation. Crystal packing of the different enantiomers results in needle-like crystals yielding CPL emission.

3 | Conclusion

In this work, we have introduced the first family of spirobisanthracene–tetraphenylethene (SBA–TPE) hybrids, expanding the structural diversity of spiro-linked π-systems. Single-crystal x-ray diffraction and theoretical studies revealed that the SBA core adopts a boat-like conformation, with enhanced twisting in derivatives bearing two TPE units. These structural features critically influence the photophysical behavior of the compounds. Both hybrids exhibit solid-state luminescence, with compound **1** delivering broadband white emission closely matching the D65 illuminant standard, while compound **2** shows intense blue emission. Time-resolved spectroscopy indicates that these emissions arise from multiple emissive states associated with distinct packing motifs and aggregate structures. Furthermore, the axial chirality of compound **2** enabled enantiomeric resolution and the observation of circularly polarized luminescence (CPL) in the solid state, with dissymmetry factors up to 10^{-3} in thin films and aggregates. This chiral emission allowed discrimination of different types of crystals according to their dissymmetry using CPL imaging. These findings demonstrate that SBA-TPE scaffolds combine structural novelty, tunable emission color, and chiroptical activity, thereby paving the way for their implementation in

advanced optoelectronic applications, including white-light OLEDs and blue CPL-OLEDs.

Author Contributions

José L. Páez: investigation, visualization, data curation, writing – review and editing. **Riccardo Rubino:** investigation, data curation, visualization. **Giulia Micolonghi:** investigation, data curation, visualization. **Marco Reale:** writing – original draft, writing – review and editing, investigation, data curation, formal analysis. **Alice Sciortino:** investigation, data curation, visualization. **Victor Blanco:** formal analysis, investigation, writing – review and editing. **Angel Orte:** supervision, resources, writing – review and editing, writing – original draft. **Carlos M. Cruz:** supervision, funding acquisition, writing – original draft, writing – review and editing, conceptualization, project administration, resources.

Acknowledgments

This research has received funding from grant PID2022-137403NA-I00 funded by MICIU/AEI/10.13039/501100011033 and by ERDF/EU; grant RYC2023-044652-I funded by MICIU/ AEI/10.13039/501100011033 and by ESF+. C.M.C. acknowledges grant PPJIA-2023.057 funded by University of Granada. J.L.P. acknowledges grant PRE2022-102320 funded by MICIU/AEI/10.13039/501100011033 and by ESF+. A.S. acknowledges Project PRIN 2022–20223CWFZT "Vertically Oriented Graphene Assembled Nanostructures for WATER purification." A.O. acknowledges funding from Universidad de Granada for the Nanoscopy-UGR Singular Laboratory. V.B. acknowledges grant PID2023-146433NB-I00 funded by MICIU/AEI/10.13039/501100011033 and "ERDF/EU". The authors would like to thank the computing time provided by the «Servicio de Supercomputación de la Universidad de Granada» (https://supercomputacion.ugr.es). Funding for open access charge: Universidad de Granada / CBUA.

Conflicts of Interest

The authors declare no conflicts of interest.

Data Availability Statement

The data that support the findings of this study are openly available in Zenodo at doi.org/10.5281/zenodo.18267874.

References

1. R. Hoffmann, A. Imamura, and G. D. Zeiss, "Spirarenes," *Journal of the American Chemical Society* 89 (1967): 5215–5220, https://doi.org/10.1021/ja00996a023.

2. H. E. Simmons and T. Fukunaga, "Spiroconjugation," *Journal of the American Chemical Society* 89 (1967): 5208–5215, https://doi.org/10.1021/ja00996a022.

3. A. Ozcelik, D. Aranda, R. Pereira-Cameselle, et al., "ON/OFF Spiroconjugation Through Peripheral Functionalization: Impact on the Reactivity and Chiroptical Properties of Spirobifluorenes," *ChemPlusChem* 87 (2022): e202100554, https://doi.org/10.1002/cplu.202100554.

4. M. Lv, X. Lu, Y. Jiang, et al., "Near-Unity Triplet Generation Promoted via Spiro-Conjugation," *Angewandte Chemie International Edition* 61 (2022): e202113190, https://doi.org/10.1002/anie.202113190.

5. T. Sakamaki, Y. Zhang, S. Fukuma, et al., "Doubly Spiro-Conjugated Chiral Carbocycles Exhibiting SOMO–HOMO Inversion in Persistent Radical Cations," *Journal of the American Chemical Society* 146 (2024): 12712–12722.

6. C. Yang, J. Cao, J.-L. Lin, H. Wu, H.-L. Zhang, and X. Guo, "Exceptional Field Effect and Negative Differential Conductance in Spiro-Conjugated Single-Molecule Junctions," *Journal of the American Chemical Society* 146 (2024): 29703–29711, https://doi.org/10.1021/jacs.4c10924.

7. Z. Yu, C. Jing, Y. Qu, et al., "Spiro-Conjugated π–σ–π Architectures Enable Single-Molecule Insulators via Destructive Quantum Interference," *Angewandte Chemie International Edition* 65 (2026): e23778.

8. S. Liu, D. Xia, and M. Baumgarten, "Rigidly Fused Spiro-Conjugated π-Systems," *ChemPlusChem* 86 (2021): 36–48.

9. Z. Hawash, L. K. Ono, and Y. Qi, "Recent Advances in Spiro-MeOTAD Hole Transport Material and its Applications in Organic–Inorganic Halide Perovskite Solar Cells," *Advanced Materials Interfaces* 5 (2018): 1700623.

10. F. M. Rombach, S. A. Haque, and T. J. Macdonald, "Lessons Learned From Spiro-OMeTAD and PTAA in Perovskite Solar Cells," *Energy & Environmental Science* 14 (2021): 5161–5190, https://doi.org/10.1039/D1EE02095A.

11. S.-Y. Jeong, H.-S. Kim, and N.-G. Park, "Challenges for Thermally Stable Spiro-MeOTAD toward the Market Entry of Highly Efficient Perovskite Solar Cells," *ACS Applied Materials & Interfaces* 14 (2022): 34220–34227, https://doi.org/10.1021/acsami.1c21852.

12. T. P. I. Saragi, T. Spehr, A. Siebert, T. Fuhrmann-Lieker, and J. Salbeck, "Spiro Compounds for Organic Optoelectronics," *Chemical Reviews* 107 (2007): 1011–1065, https://doi.org/10.1021/cr0501341.

13. J. Ramakrishna and P. Venkatakrishnan, "Bigger and Brighter Fluorenes: Facile π-Expansion, Brilliant Emission and Sensing of Nitroaromatics," *Chemistry-An Asian Journal* 12 (2017): 181–189, https://doi.org/10.1002/asia.201601359.

14. Y. Hu, D. Wang, M. Baumgarten, D. Schollmeyer, K. Müllen, and A. Narita, "Spiro-Fused Bis-hexa-*peri*-hexabenzocoronene," *Chemical Communications* 54 (2018): 13575–13578.

15. J. Feng, L. Fu, H. Geng, W. Jiang, and Z. Wang, "Designing a Near-Infrared Circularly Polarized Luminescent Dye by Dissymmetric Spiro-Fusion," *Chemical Communications* 56 (2020): 912–915, https://doi.org/10.1039/C9CC08619F.

16. P. Izquierdo-García, J. M. Fernández-García, J. Perles, I. Fernández, and N. Martín, "Electronic Control of the Scholl Reaction: Selective Synthesis of Spiro vs Helical Nanographenes," *Angewandte Chemie International Edition* 62 (2023): e202215655, https://doi.org/10.1002/anie.202215655.

17. K. Song, Y. Zhang, S. Wu, et al., "Spiro-Fused Dibenzo[g, p]Chrysene: Annulative π-Extension (APEX) Synthesis and Properties," *Organic Chemistry Frontiers* 12 (2025): 2225–2231, https://doi.org/10.1039/D4QO02104E.

18. J. Lión-Villar, J. M. Fernández-García, S. M. Rivero, et al., "Synthesis of Zwitterionic Open-Shell Bilayer Spironanographenes," *Nature Chemistry* 17 (2025): 1099–1106, https://doi.org/10.1038/s41557-025-01810-2.

19. V. Kumar, S. D. Dongre, A. Vandhanam, A. B. Jadhav, J. Kumar, and S. S. Babu, "(Chiro)optical Properties of π-Extended Spiro-Double Carbo[7]Helicene," *Journal of Physical Chemistry Letters* 16 (2025): 11657–11664, https://doi.org/10.1021/acs.jpclett.5c02897.

20. L. J. Sicard, H. Li, Q. Wang, et al., "C1-Linked Spirobifluorene Dimers: Pure Hydrocarbon Hosts for High-Performance Blue Phosphorescent OLEDs," *Angewandte Chemie International Edition* 58 (2019): 3848–3853, https://doi.org/10.1002/anie.201813604.

21. D. Ari, Y. Yang, C. Quinton, Z. Jiang, D. Zhou, and C. Poriel, "Spirobifluorene Trimers: High Triplet Pure Hydrocarbon Hosts for Highly Efficient Blue Phosphorescent Organic Light-Emitting Diodes," *Angewandte Chemie International Edition* 63 (2024): e202403066, https://doi.org/10.1002/anie.202403066.

22. Y. Yang, D. Ari, Z. Yu, et al., "Pure Hydrocarbon Hosts Enabling Efficient Multi-Resonance TADF Blue-Emitting Organic Light-Emitting Diodes," *Angewandte Chemie International Edition* 64 (2025): e202501895, https://doi.org/10.1002/anie.202501895.

23. M. Lv, Y. Yu, M. E. Sandoval-Salinas, et al., "Engineering the Charge-Transfer State to Facilitate Spin–Orbit Charge Transfer Inter-

system Crossing in Spirobis[anthracene]Diones," *Angewandte Chemie International Edition* 59 (2020): 22179–22184.

24. K. Hasebe, K. Itami, and H. Ito, "Synthesis, Structures, and Properties of Polybenzo[n]Spirenes With Carbon-Based Polyspiroconjugation," *Organic Letters* 27 (2025): 11832–11836, https://doi.org/10.1021/acs.orglett.5c03654.

25. G. Huang, X. Du, H. Bo, and B. S. Li, "Colorful Variation of Tetraphenylethene Derivatives in the Solid state," *Materials Chemistry Frontiers* 8 (2024): 104–132, https://doi.org/10.1039/D3QM00621B.

26. Y. Hong, J. W. Y. Lam, and B. Z. Tang, "Aggregation-Induced Emission," *Chemical Society Reviews* 40 (2011): 5361, https://doi.org/10.1039/c1cs15113d.

27. J. Mei, N. L. C. Leung, R. T. K. Kwok, J. W. Y. Lam, and B. Z. Tang, "Aggregation-Induced Emission: Together We Shine, United We Soar!," *Chemical Reviews* 115 (2015): 11718–11940, https://doi.org/10.1021/acs.chemrev.5b00263.

28. G. R. Suman, M. Pandey, and A. S. J. Chakravarthy, "Review on New Horizons of Aggregation Induced Emission: From Design to Development," *Materials Chemistry Frontiers* 5 (2021): 1541–1584.

29. D. Li, R. Zuo, J. Wang, and Z. Le, "The Designs and Applications of Tetraphenylethylene Macrocycles and Cages," *Chemistry–A European Journal* 31 (2025): e202403715, https://doi.org/10.1002/chem.202403715.

30. Z. Zhao, S. Chen, X. Shen, et al., "Aggregation-Induced Emission, Self-Assembly, and Electroluminescence of 4,4′-bis(1,2,2-triphenylvinyl)Biphenyl," *Chemical Communications* 46 (2010): 686–688, https://doi.org/10.1039/B915271G.

31. J. Huang, N. Sun, Y. Dong, et al., "Similar or Totally Different: The Control of Conjugation Degree Through Minor Structural Modifications, and Deep-Blue Aggregation-Induced Emission Luminogens for Non-Doped OLEDs," *Advanced Functional Materials* 23 (2013): 2329–2337, https://doi.org/10.1002/adfm.201202639.

32. J. Huang, X. Yang, J. Wang, et al., "New Tetraphenylethene-Based Efficient Blue Luminophors: Aggregation Induced Emission and Partially Controllable Emitting Color," *Journal of Materials Chemistry* 22 (2012): 2478–2484, https://doi.org/10.1039/C1JM14054J.

33. S.-Y. Yang, J. Wang, Z. Deng, et al., "Spiro-Materials With Aggregation-Induced Emission," *Matter* 7 (2024): 3390–3421.

34. E. Vinegrad, U. Hananel, G. Markovich, and O. Cheshnovsky, "Determination of Handedness in a Single Chiral Nanocrystal via Circularly Polarized Luminescence," *ACS Nano* 13 (2019): 601–608, https://doi.org/10.1021/acsnano.8b07581.

35. P. Stachelek, L. MacKenzie, D. Parker, and R. Pal, "Circularly Polarised Luminescence Laser Scanning Confocal Microscopy to Study Live Cell Chiral Molecular Interactions," *Nature Communications* 13 (2022): 553, https://doi.org/10.1038/s41467-022-28220-z.

36. P. Stachelek, S. Serrano-Buitrago, B. L. Maroto, R. Pal, and S. de la Moya, "Circularly Polarized Luminescence Bioimaging Using Chiral BODIPYs: A Model Scaffold for Advancing Unprecedented CPL Microscopy Using Small Full-Organic Probes," *ACS Applied Materials & Interfaces* 16 (2024): 67246–67254, https://doi.org/10.1021/acsami.4c14127.

37. Z. M. Holubec and J. Jonas, "Magnetic Resonance Study of Conformation Inversion in Some Substituted 10,10-dimethyl-9,10-dihydroanthracenes," *Journal of the American Chemical Society* 90 (1968): 5986–5991, https://doi.org/10.1021/ja01024a007.

38. Deposition numbers 2525149 (for **1**) and 2525150 (for **2**) contain the supplementary crystallographic data for this paper. These data are provided free of charge by the joint Cambridge Crystallographic Data Centre and Fachinformationszentrum Karlsruhe Access Structures service.

39. W. W. H. Lee, Z. Zhao, Y. Cai, et al., "Facile Access to Deep Red/Near-Infrared Emissive AIEgens for Efficient Non-Doped OLEDs," *Chemical Science* 9 (2018): 6118–6125, https://doi.org/10.1039/C8SC01377B.

40. B. Kumari, R. Dahiwadkar, and S. Kanvah, "White Light Emission From AIE-Active Luminescent Organic Materials," *Aggregate* 3 (2022): e191.

41. Y. Nakagawa, K. Kinoshita, M. Kasuno, et al., "White Light Emission Generated by Two Stacking Patterns of a Single Organic Molecular Crystal," *Materials Advances* 3 (2022): 6466–6473, https://doi.org/10.1039/D2MA00670G.

42. S. I. Hintschich, C. Rothe, S. M. King, S. J. Clark, and A. P. Monkman, "The Complex Excited-State Behavior of a Polyspirobifluorene Derivative: The Role of Spiroconjugation and Mixed Charge Transfer Character on Excited-State Stabilization and Radiative Lifetime," *Journal of Physical Chemistry B* 112 (2008): 16300–16306, https://doi.org/10.1021/jp8044884.

43. A. Kabro, T. Roisnel, C. Fischmeister, and C. Bruneau, "Ruthenium–Indenylidene Olefin Metathesis Catalyst With Enhanced Thermal Stability," *Chemistry–A European Journal* 16 (2010): 12255–12261.

44. Y. Zhang, X. Li, Q. Mo, W. Shi, J. Zhao, and S. Zhu, "Highly Regioselective Cobalt-Catalyzed Hydroboration of Internal Alkynes," *Angewandte Chemie International Edition* 61 (2022): e202208473, https://doi.org/10.1002/anie.202208473.

45. G. M. Sheldrick, "*SHELXT*—Integrated Space-Group and Crystal-Structure Determination," *Acta Crystallographica* A71 (2015): 3–8.

46. G. M. Sheldrick, "Crystal Structure Refinement With *SHELXL*," *Acta Crystallographica* C71 (2015): 3–8.

47. G. M. Sheldrick, "A Short History of *SHELX*," *Acta Crystallographica* A64 (2008): 112–122.

48. L. J. Farrugia, "*WinGX* and *ORTEP for Windows* : An Update," *Journal of Applied Crystallography* 45 (2012): 849–854.

49. A. L. Spek, "Platon Squeeze: A Tool for the Calculation of the Disordered Solvent Contribution to the Calculated Structure Factors," *Acta Crystallographica* C71 (2015): 9–18.

50. A. L. Spek, "Structure Validation in Chemical Crystallography," *Acta Crystallographica* D65 (2009): 148–155.

51. O. V. Dolomanov, L. J. Bourhis, R. J. Gildea, J. A. K. Howard, and H. Puschmann, "OLEX2: A Complete Structure Solution, Refinement and Analysis Program," *Journal of Applied Crystallography* 42 (2009): 339–341, https://doi.org/10.1107/S0021889808042726.

Supporting Information

Additional supporting information can be found online in the Supporting Information section.

Supporting File 1: The authors have cited additional references within the Supporting Information [43–51].

Supporting File 2: anie72457-sup-0002-cif.zip.